EURODINAME III - An International Symposium on Dynamic Problems of Mechanics
June 8-11, 2026 - Giens Peninsula, FR

EURODINAME-2026-13481
UNCERTAINTY QUANTIFICATION OF A BEAM-LIKE PHONONIC CRYSTAL WITH ATTACHED COMPOSITE PATCHES

Yuri Andrade Dias Martins
Aeronautics Institute of Technology, Praça Marechal Eduardo Gomes, 50 – São José dos Campos, 12228-900, SP, Brazil
yurimartins@ita.br

Vinícius Mauro de Souza Santos
Aeronautics Institute of Technology, Praça Marechal Eduardo Gomes, 50 – São José dos Campos, 12228-900, SP, Brazil
Université Marie et Louis Pasteur, SUPMICROTECH, CNRS, Institut FEMTO-ST, Besançon, F-25000, France
vinicius.santos@ga.ita.br, vinicius.mauro@femto-st.fr

Gabriel Rodrigues Dias
Thiago de Paula Sales
Domingos Alves Rade
Aeronautics Institute of Technology, Praça Marechal Eduardo Gomes, 50 – São José dos Campos, 12228-900, SP, Brazil
gabriel.dias.101863@ga.ita.br, tpsales@ita.br, thiago.sales@gp.ita.br, domingos.rade@gp.ita.br

Abstract. *Periodic structures have attracted increasing interest lately due to their unique wave propagation characteristics. Although widely studied, uncertainty quantification of their dynamic behavior remains almost not explored. Hence, this work investigates the impact of manufacturing and material uncertainties on the bandgaps of a beam-like phononic crystal (PC) with composite patches attached to the beam using structural adhesive. Randomnesses in the patch gluing position, stack angle of layers, and material properties of the structural adhesive are taken into account using prescribed probability distribution functions. The composite laminate patches are modeled using equivalent single-layer theory, while the beam–patch interactions is based on a layer-wise multilayer beam model, which considers Zig-Zag kinematics. The Spectral Element Method and Monte Carlo (MC) simulations are used to evaluate the stochastic dynamic responses. Stochastic transmissibility functions are afterwards obtained to assess the influences of input random variables on the beam's first bending bandgap. The results reveal that the combined source of uncertainties in the patch gluing position, stack angle of layers, and material properties of the structural adhesive are relevant for the PC dynamic behavior.*

Keywords: *phononic crystal, spectral element method, manufacturing variability, periodic structures, bandgap*

1. INTRODUCTION

Vibration reduction has become a key driver for advancements in civil, mechanical, and aerospace engineering. In this context, periodic structures have been shown to possess unique properties for wave manipulation (Zhang *et al.*, 2024; Korshunova *et al.*, 2021). Periodic media comprise either materials with an underlying microstructural periodicity or structural systems assembled from repeating substructures, commonly referred to as unit cells. They are known to exhibit bandgaps, i.e., frequency ranges in which wave propagation is prohibited. This property enables periodic structures to function as frequency filters and vibration isolators (Zhang *et al.*, 2018).

Several studies have explored periodic structures for vibration mitigation. Jin *et al.* (2022) designed a vibration isolator based on phononic crystals. Billon *et al.* (2017) investigated bandgaps in auxetic composite metamaterials. Bishay and Rodriguez (2021) examined the dynamic response of periodic fiber-reinforced laminated composite beams. Bishay and Amirbekyan (2021) proposed a design approach for periodic laminated composite beams aimed at tuning bandgaps.

However, achieving a perfectly periodic architecture is challenging due to unavoidable uncertainties. For instance, material properties may deviate from their nominal values, and structural dimensions may vary as a result of inherent manufacturing variability. Consequently, numerous studies have incorporated variabilities into the design process and the structural dynamic behavior of such systems (Huang *et al.*, 2007; Salatovic *et al.*, 2025; Lee and Kim, 2000).

This work is licensed under a Creative Commons "Attribution 4.0 International" license.

Fabro *et al.* (2020) investigated the effects of the variabilities generated by additive manufacturing process of a periodic structure. Ribeiro *et al.* (2024) presented an optimization approach for designing a periodic structure that take into account the uncertainties of manufacturing process. Souza *et al.* (2020) used a Bayesian framework to study the effects of manufacturing variability on the effective wavenumber identification in beams with evenly attached resonators. Agrawal *et al.* (2022) used robust topology optimization to design negative Poisson's ratio metamaterials considering material uncertainties. Sharma *et al.* (2020) developed stochastic models based on polynomial chaos expansion theory and MC simulations to investigate the acoustic performance of an underwater coating considering uncertainty in material and geometric properties. Santos *et al.* (2025) investigated the dynamic behavior of a beam-like periodic structure under the presence of environmental and boundary condition randomness.

Within the framework outlined above, this paper conducts uncertainty quantification of the central frequency and bandwidth of the first bending bandgap of the beam-like PC with attached composite patches shown in Fig. 1a. Three sources of uncertainty associated with manufacturing and material variability are considered: i) randomness in the stacking angle (SA) $\phi^{(k)}(\theta)$ (Fig. 1b), ii) randomness in the patch gluing position (Fig. 1c), and iii) randomness in the adhesive material properties (Fig. 1d). One should mention that θ is employed in Fig. 1 and throughout the text to denote random quantities that belong to appropriate sample spaces.

This paper is structured as follows. In Section 2, the equivalent single-layer model for the laminate patches and the spectral element modeling of multilayer beams is presented; in Section 3, first, the deterministic analysis regarding dispersion curves and transmissiblity function is outlined, considering the mean value of the stochastic parameters, and afterwards the individual influence of each random variable is assessed, followed by the combined randomness of all sources; in Section 4, main conclusions drawn from the study are presented, highlighting the key findings; acknowledgments and references come afterward.

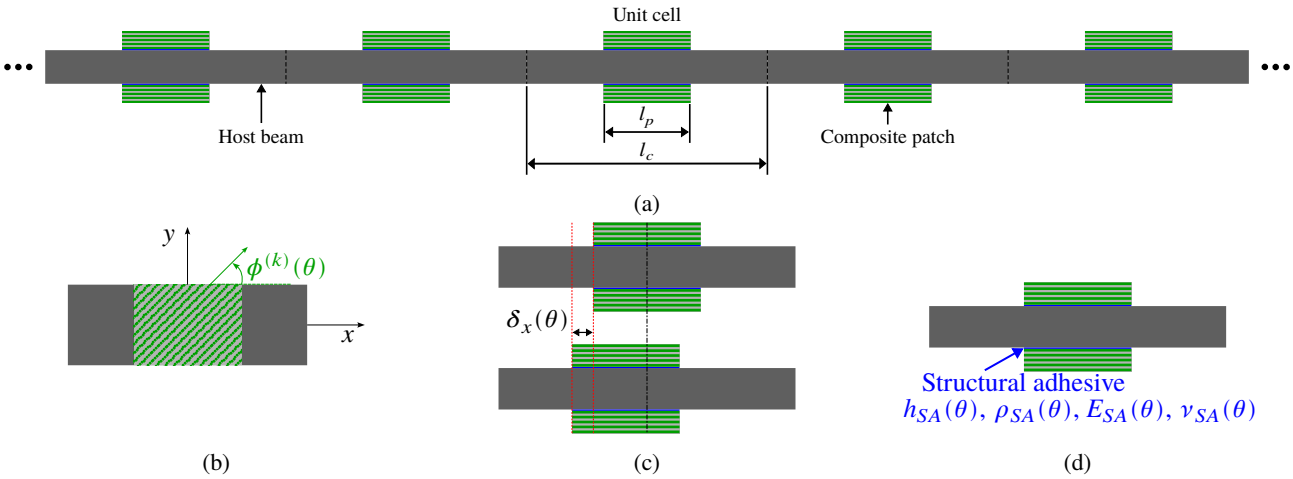


Figure 1: Problem statement: a) infinite, homogeneous host beam periodically covered by composite patches; and randomness in the b) stacking angle and c) gluing position of composite patches, and d) material properties of structural adhesive.

2. MATHEMATICAL MODELING

In this section, the modeling background of periodic structures such as that illustrated in Fig. 1a is presented. Initially, a mathematical framework is developed in Section 2.1 to describe N-layered composite beams (utilized for modeling the composite patches) based in the first-order shear deformation theory (FSDT) alongside the extended Timoshenko beam theory (ETBT) (Birman and Kardomateas, 2018). The considered framework utilizes an equivalent single layer (ESL) (Reddy, 2003; Abrate and Di Sciuva, 2017) to characterize each composite patch as a single lamina with equivalent inertial and elastic properties. Subsequently, to analyze the modeling of wave propagation phenomena within a complete unit cell (refer to Fig. 1a), which comprises three beam segments, with the central segment being multilayered, conventional SEM procedures are employed, incorporating an exact model based on Zig-Zag kinematics (Carrera, 2003), as elucidated in Section 2.2. Finally, the dynamic behavior of infinite and finite multilayer periodic beams is addressed in Section 2.3.

2.1 Equivalent single-layer model for the laminate patches

The constitutive stress-strain relations for the k-th orthotropic lamina of a composite patch with length L, width b, and height h, as shown in Fig. 2, can be written as (Lee, 2009; Reddy, 2003):

$$\begin{Bmatrix} \sigma_{xx}^{(k)}(\theta) \\ \sigma_{yy}^{(k)}(\theta) \\ \sigma_{xy}^{(k)}(\theta) \\ \sigma_{yz}^{(k)}(\theta) \\ \sigma_{zx}^{(k)}(\theta) \end{Bmatrix} = \mathbf{T}_K^{(k)}(\theta) \begin{bmatrix} \frac{E_1^{(k)}}{1-\nu_{12}^{(k)}\nu_{21}^{(k)}} & \frac{\nu_{12}^{(k)}E_2^{(k)}}{1-\nu_{12}^{(k)}\nu_{21}^{(k)}} & 0 & 0 & 0 \\ \frac{\nu_{12}^{(k)}E_2^{(k)}}{1-\nu_{12}^{(k)}\nu_{21}^{(k)}} & \frac{E_2^{(k)}}{1-\nu_{12}^{(k)}\nu_{21}^{(k)}} & 0 & 0 & 0 \\ 0 & 0 & G_{12}^{(k)} & 0 & 0 \\ 0 & 0 & 0 & G_{23}^{(k)} & 0 \\ 0 & 0 & 0 & 0 & G_{31}^{(k)} \end{bmatrix} \mathbf{T}_K^{(k)\mathrm{T}}(\theta) \begin{Bmatrix} \epsilon_{xx}^{(k)} \\ \epsilon_{yy}^{(k)} \\ 2\epsilon_{xy}^{(k)} \\ 2\epsilon_{yz}^{(k)} \\ 2\epsilon_{zx}^{(k)} \end{Bmatrix}, \tag{1}$$

where $\epsilon_{ij}^{(k)}$ and $\sigma_{ij}^{(k)}(\theta)$, $ij \in \{xx, yy, xy, yz, zx\}$, represent components of the strain and stochastic stress tensors referred to the global coordinate system,

$$\mathbf{T}_K^{(k)}(\theta) = \begin{bmatrix} c_{\phi^{(k)}}^2(\theta) & s_{\phi^{(k)}}^2(\theta) & -2s_{\phi^{(k)}}(\theta)c_{\phi^{(k)}}(\theta) & 0 & 0 \\ s_{\phi^{(k)}}^2(\theta) & c_{\phi^{(k)}}^2(\theta) & 2s_{\phi^{(k)}}(\theta)c_{\phi^{(k)}}(\theta) & 0 & 0 \\ s_{\phi^{(k)}}(\theta)c_{\phi^{(k)}}(\theta) & -s_{\phi^{(k)}}(\theta)c_{\phi^{(k)}}(\theta) & c_{\phi^{(k)}}^2(\theta) - s_{\phi^{(k)}}^2(\theta) & 0 & 0 \\ 0 & 0 & 0 & c_{\phi^{(k)}}(\theta) & s_{\phi^{(k)}}(\theta) \\ 0 & 0 & 0 & -s_{\phi^{(k)}}(\theta) & c_{\phi^{(k)}}(\theta) \end{bmatrix}, \tag{2}$$

being $\phi^{(k)}(\theta)$ the stochastic orientation angle of the k-th lamina (see Fig. 2), with $c_{\phi^{(k)}}(\theta) \equiv \cos\phi^{(k)}(\theta)$ and $s_{\phi^{(k)}}(\theta) \equiv \sin\phi^{(k)}(\theta)$, and $E_1^{(k)}$, $E_2^{(k)}$, $G_{12}^{(k)}$, $G_{23}^{(k)}$, $G_{31}^{(k)}$, $\nu_{12}^{(k)}$, and $\nu_{21}^{(k)}$ representing the Young's moduli, shear moduli, and Poisson's ratios of the lamina, associated with the local directions $(1, 2)$. One notes that time and space dependencies are omitted in Eq. (1). It should be clarified that the stress component σ_{zz} is assumed null, as the total thickness of the laminate is considered to be much smaller than its other dimensions.

Integrating the stochastic stresses provided in Eq. (1) over the laminate thickness, one obtains the stochastic in-plane resultant forces $\mathbf{n}(\theta) = \begin{Bmatrix} N_{xx}(\theta) & N_{yy}(\theta) & N_{xy}(\theta) \end{Bmatrix}^{\mathrm{T}}$, moments $\mathbf{m}(\theta) = \begin{Bmatrix} M_{xx}(\theta) & M_{yy}(\theta) & M_{xy}(\theta) \end{Bmatrix}^{\mathrm{T}}$, and transverse shear forces $\overline{\mathbf{q}}(\theta) = \begin{Bmatrix} \overline{Q}_y(\theta) & \overline{Q}_x(\theta) \end{Bmatrix}^{\mathrm{T}}$, all per unit length, being given by:

$$\begin{Bmatrix} \mathbf{n}(\theta) \\ \mathbf{m}(\theta) \\ \overline{\mathbf{q}}(\theta) \end{Bmatrix} = \underbrace{\begin{bmatrix} \mathbf{A}(\theta) & \mathbf{B}(\theta) & \mathbf{0} \\ \mathbf{B}(\theta) & \mathbf{D}(\theta) & \mathbf{0} \\ \mathbf{0} & \mathbf{0} & \overline{\mathbf{A}}(\theta) \end{bmatrix}}_{\mathbf{K}(\theta)} \begin{Bmatrix} \boldsymbol{\varepsilon}_1 \\ \boldsymbol{\varepsilon}_2 \\ \boldsymbol{\varepsilon}_3 \end{Bmatrix}, \quad \boldsymbol{\varepsilon}_1 = \begin{Bmatrix} \partial u_c/\partial x \\ \partial v_c/\partial y \\ \frac{\partial u_c}{\partial y} + \frac{\partial v_c}{\partial x} \end{Bmatrix}, \quad \boldsymbol{\varepsilon}_2 = \begin{Bmatrix} \partial \psi_x/\partial x \\ \partial \psi_y/\partial y \\ \frac{\partial \psi_x}{\partial y} + \frac{\partial \psi_y}{\partial x} \end{Bmatrix}, \quad \boldsymbol{\varepsilon}_3 = \begin{Bmatrix} \frac{\partial w}{\partial y} + \psi_y \\ \frac{\partial w}{\partial x} + \psi_x \end{Bmatrix}, \tag{3}$$

where u_c, v_c, and $w_c \equiv w$ denote displacements of a point at $z = 0$ along x, y, and z, and ψ_x, ψ_y represent the cross-section rotations about y and x, respectively. In Eq. (3), the stochastic matrices $\mathbf{A}(\theta)$, $\mathbf{B}(\theta)$, $\mathbf{D}(\theta)$, and $\overline{\mathbf{A}}(\theta)$ collect extensional, bending-extensional coupling, bending, and shear-related extensional stiffness coefficients (Reddy, 2003).

To particularize Eq. (3) for the cases of interest, which concern beams under plane-stress condition, the resultants $N_{yy}(\theta)$, $N_{xy}(\theta)$, $M_{yy}(\theta)$, $M_{xy}(\theta)$, and $\overline{Q}_y(\theta)$ are all taken to be nil. Thus, one can partition $\mathbf{K}(\theta)$ in Eq. (3) according to the sets r and c of retained and to-be-condensed laminate strains. This condensation procedure leads to:

$$\begin{Bmatrix} N_{xx}(\theta) \\ \overline{Q}_x(\theta) \\ M_{xx}(\theta) \end{Bmatrix} = \overline{\mathbf{K}}(\theta) \begin{Bmatrix} \partial u_c/\partial x \\ \frac{\partial w}{\partial x} + \psi_x \\ \partial \psi_x/\partial x \end{Bmatrix} = \overline{\mathbf{K}}(\theta) \begin{Bmatrix} u_c' \\ \gamma_{xy} \\ \psi_x' \end{Bmatrix}, \qquad \text{with} \qquad \overline{\mathbf{K}}(\theta) = \mathbf{K}_{rr}(\theta) - \mathbf{K}_{rc}(\theta)\mathbf{K}_{cc}(\theta)^{-1}\mathbf{K}_{cr}(\theta), \tag{4}$$

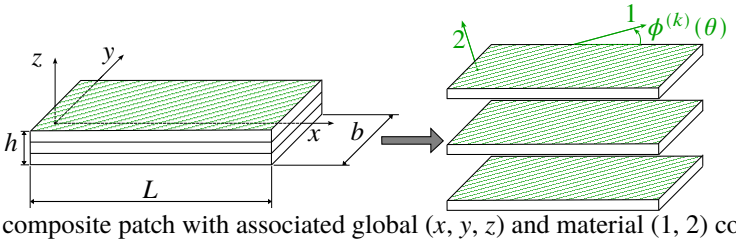


Figure 2: Laminate composite patch with associated global (x, y, z) and material (1, 2) coordinate systems.

where $\mathbf{K}_{rr}(\theta)$, $\mathbf{K}_{rc}(\theta)$, $\mathbf{K}_{cr}(\theta)$, and $\mathbf{K}_{cc}(\theta)$ are partitions of $\mathbf{K}(\theta)$, and $\overline{\mathbf{K}}(\theta)$ denotes the stochastic effective stiffness of the composite laminate beam patch.

Equivalent single layer stochastic properties can then be determined for the composite patch from entries of $\overline{\mathbf{K}}(\theta)$ as follows:

$$\begin{aligned} EA_{eq}(\theta) &= b\overline{K}_{11}(\theta), \quad \kappa GA_{eq}(\theta) = \kappa b\overline{K}_{22}(\theta), \quad EI_{eq}(\theta) = b\overline{K}_{33}(\theta), \\ C_1(\theta) &= b\overline{K}_{12}(\theta), \quad C_2(\theta) = -b\overline{K}_{13}(\theta), \quad C_3(\theta) = b\overline{K}_{23}(\theta), \end{aligned} \tag{5}$$

where the subscript eq indicates equivalent rigidity properties, with $EA_{eq}(\theta)$ denoting the extensional rigidity, $EI_{eq}(\theta)$ the flexural bending rigidity, $\kappa GA_{eq}(\theta)$ the shear rigidity, accounting for a shear correction factor, and $C_1(\theta)$, $C_2(\theta)$, and $C_3(\theta)$ the coupling rigidities (Lee, 2009), respectively.

Furthermore, equivalent inertial properties for the composite patch can be computed as follows:

$$\rho A_{eq} = b^{(k)} \sum_{k=1}^{N_\mathrm{p}} \rho^{(k)} \left[z^{(k)} - z^{(k-1)} \right], \; \rho R_{eq} = \frac{b^{(k)}}{2} \sum_{k=1}^{N_\mathrm{p}} \rho^{(k)} \left[{z^{(k)}}^2 - {z^{(k-1)}}^2 \right], \; \rho I_{eq} = \frac{b^{(k)}}{3} \sum_{k=1}^{N_\mathrm{p}} \rho^{(k)} \left[{z^{(k)}}^3 - {z^{(k-1)}}^3 \right], \tag{6}$$

where $z^{(k)}$, $z^{(k-1)}$ denote the z coordinates corresponding to the interfaces of the k-th lamina; N_p stands for the number of laminae making up the laminate; ρA_{eq} stands for the apparent mass associated with the composite patch, ρR_{eq} corresponds to the apparent first-order mass moment of inertia about the y-axis, and ρI_{eq} identifies the apparent second-order mass moment of inertia about the same axis. It should be clarified that unlike the equivalent composite elastic properties (cf. Eq. (5)), the inertial ones are not affected by randomness since $b^{(k)}$, $\rho^{(k)}$ and $z^{(k)}$ are not considered as stochastic quantities for the composite patches.

2.2 Spectral element modeling of multilayer beams featuring composite patches

Having the equivalent single-layer governing equations for laminate composite patches, the interest is to model the wave propagation behavior of multilayered beams, which can possibly combine laminate composite and metallic layers, as depicted in Fig. 1a, by making use of the Zig-Zag theory (Unal *et al.*, 2016; Banerjee *et al.*, 2007).

Figure 3 shows an N_b-layered beam with total length L. The relevant properties of the layers, which are numbered $l = 1, 2, ..., N_\mathrm{b}$ bottom to top, are also indicated: thicknesses $h^{(N_\mathrm{b})}$, widths $b^{(N_\mathrm{b})}$, centroidal second moments of area y, $I_y^{(N_\mathrm{b})}$, volumetric densities $\rho^{(N_\mathrm{b})}$, Young's moduli $E^{(N_\mathrm{b})}$, cross-sectional areas $A^{(N_\mathrm{b})}$, shear moduli $G^{(N_\mathrm{b})}$, shear correction factors $\kappa^{(N_\mathrm{b})}$, and Poisson's ratios $\nu^{(N_\mathrm{b})}$.

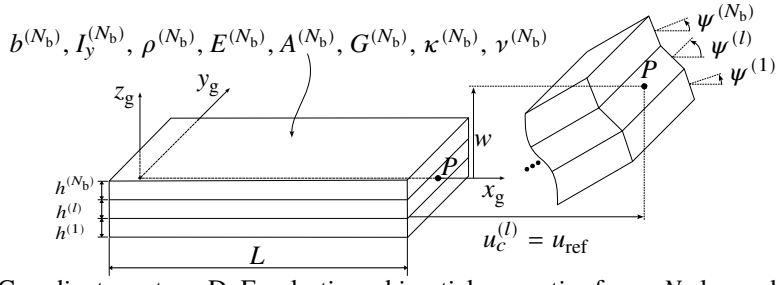


Figure 3: Coordinate system, DoFs, elastic and inertial properties for an N_b-layered beam.

The Zig-Zag theory assumes that displacements and strains are small so that linear elasticity holds. Moreover, the hypothesis of perfect continuity of displacements across interfaces is considered, leading to no slippage or delamination during deformation. Furthermore, the transversal displacement w along the z_g–axis is constant across all layers, whereas axial displacements (along the x_g–axis) and rotations of cross-sections differ for each layer. Additionally, each layer deforms according to the Timoshenko beam theory, such that in-plane shear strain and cross-section rotational inertia are both accounted for. The total strain and kinetic energies associated with an N_b-layered beam can be expressed, respectively, as (Lee, 2009):

$$U(\theta) = \frac{1}{2} \sum_{l=1}^{N_\mathrm{b}} \int_0^L \begin{Bmatrix} u_c'^{(l)} \\ \gamma_{xy}^{(l)} \\ \psi'^{(l)} \end{Bmatrix}^\mathrm{T} \begin{bmatrix} EA_{eq}^{(l)}(\theta) & C_1^{(l)}(\theta) & C_2^{(l)}(\theta) \\ C_1^{(l)}(\theta) & \kappa GA_{eq}^{(l)}(\theta) & C_3^{(l)}(\theta) \\ C_2^{(l)}(\theta) & C_3^{(l)}(\theta) & EI_{eq}^{(l)}(\theta) \end{bmatrix} \begin{Bmatrix} u_c'^{(l)} \\ \gamma_{xy}^{(l)} \\ \psi'^{(l)} \end{Bmatrix} \mathrm{d}x, \tag{7}$$

$$T(\theta) = \frac{1}{2} \sum_{l=1}^{N_\mathrm{b}} \int_0^L \begin{Bmatrix} \dot{u}_c^{(l)} \\ \dot{w} \\ \dot{\psi}^{(l)} \end{Bmatrix}^\mathrm{T} \begin{bmatrix} \rho A_{eq}^{(l)}(\theta) & 0 & \rho R_{eq}^{(l)}(\theta) \\ 0 & \rho A_{eq}^{(l)}(\theta) & 0 \\ \rho R_{eq}^{(l)}(\theta) & 0 & \rho I_{eq}^{(l)}(\theta) \end{bmatrix} \begin{Bmatrix} \dot{u}_c^{(l)} \\ \dot{w} \\ \dot{\psi}^{(l)} \end{Bmatrix} \mathrm{d}x, \tag{8}$$

where overdots indicate time differentiation. Although the equivalent inertial properties from Eq. (6) are not affected by randomness, the ones presented in Eq. (8) are stochastic quantities. Their difference lies in the fact that, for the multilayer beam, one aims to study the effects of randomness in the structural adhesive that bonds the composite patches to the metallic host beam. In this way, in addition to equivalent single-layers for the laminate patches and a corresponding layer for the metallic host beam, additional thin layers are considered to model the structural adhesive above and below the host beam, whose properties are assumed to be uncertain, since they are hard to control, as indicated in Fig. 1d. In particular, $h_{SA}(\theta)$ denotes the stochastic structural adhesive thickness due to manufacturing imperfections; $\rho_{SA}(\theta)$ stands for the stochastic volumetric density; $E_{SA}(\theta)$ corresponds to the stochastic Young's modulus; and $\nu_{SA}(\theta)$ identifies the stochastic Poisson's ratio. The three later properties are associated with material quality uncertainties. Having U and T, Hamilton's principle can be evoked to derive the partial differential equations governing the motion of the multilayer beam, as well as the associated geometric and natural boundary conditions that apply to the problem. This has been accomplished by recurring to the MATLAB® Symbolic Math Toolbox.

Following the theory previously presented, to assemble the global set of equations of motion describing the unit cell identified in Fig. 1a, three spectral finite elements have to be coupled, two of which degenerate into simple, single-layered Timoshenko beam elements. For clarification, Fig. 4 illustrates the DoFs involved in the enforcement of continuity conditions, considering that each node has, as independent DoFs: the axial displacement of the middle plane of the complete multilayer arrangement, the beam transverse displacement, and the individual rotations of the cross-sections of all layers. Instead of directly coupling those DoFs that are shared between elements by eliminating redundant ones, the option was made to adjoin algebraic continuity constraint equations to the full set of frequency-domain SEM equations, making use of Lagrange multipliers. Accordingly, the DoFs of element 2 indicated in blue were treated as dependent, while the remaining ones were considered independent. This strategy becomes advantageous as it allows for generalizing and facilitating the enforcement of continuity-related constraint equations related to multilayer beams that are not symmetric, for example.

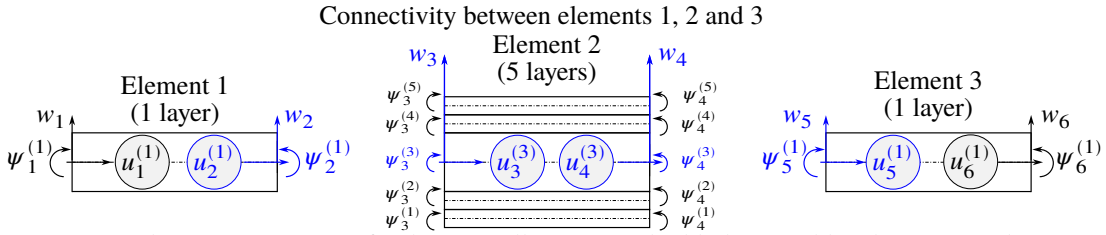


Figure 4: Element connectivity for the unit cell in Fig. 1a, highlighting in blue the connected DoFs.

Hence, the frequency domain equations to be solved are obtained as:

$$\begin{bmatrix} \bar{\mathbf{S}}(\theta) & \mathbf{C}_{\bar{\mathbf{Q}}(\theta)}^{\mathrm{T}} \\ \mathbf{C}_{\bar{\mathbf{Q}}(\theta)} & \mathbf{0} \end{bmatrix} \begin{Bmatrix} \bar{\mathbf{Q}}(\theta) \\ \boldsymbol{\lambda}(\theta) \end{Bmatrix} = \begin{Bmatrix} \bar{\mathbf{F}} \\ \mathbf{0} \end{Bmatrix}, \tag{9}$$

where $\bar{\mathbf{S}}(\theta)$ is symmetric, stochastic and frequency-dependent; $\mathbf{C}_{\bar{\mathbf{Q}}(\theta)}$ is an $m \times n$ Jacobian matrix of m non-redundant constraints; $\boldsymbol{\lambda}(\theta)$ denotes a vector of m Lagrange multipliers; $\bar{\mathbf{Q}}(\theta)$ collects the stochastic frequency-dependent, potentially complex amplitudes of the n nodal DoFs depicted in Fig. 4; and $\bar{\mathbf{F}}$ contains the spectrum amplitudes of the externally applied loads.

By suitably identifying a subset of DoFs as dependent, such as those belonging to element 2 that are highlighted in blue in Fig. 4, one can partition $\bar{\mathbf{Q}}(\theta)$ by considering sets of dependent (d) and independent (i) DoFs. Accordingly, $\mathbf{C}_{\bar{\mathbf{Q}}(\theta)}$ can be partitioned to provide $\mathbf{C}_{\bar{\mathbf{Q}}_d(\theta)}$, which is $m \times m$, and $\mathbf{C}_{\bar{\mathbf{Q}}_i(\theta)}$, of size $m \times (n-m)$. Since the constraint equations are assumed to be non-redundant and the selected dependent DoFs are suitably chosen, $\mathbf{C}_{\bar{\mathbf{Q}}_d(\theta)}$ has an inverse, such that, from the second set of equations appearing in Eq. (9):

$$\bar{\mathbf{Q}}_d(\theta) = -\mathbf{C}_{\bar{\mathbf{Q}}_d(\theta)}^{-1} \mathbf{C}_{\bar{\mathbf{Q}}_i(\theta)} \bar{\mathbf{Q}}_i(\theta) \qquad \Rightarrow \qquad \bar{\mathbf{Q}}(\theta) = \begin{Bmatrix} \bar{\mathbf{Q}}_i(\theta) \\ \bar{\mathbf{Q}}_d(\theta) \end{Bmatrix} = \begin{bmatrix} \mathbf{I} \\ -\mathbf{C}_{\bar{\mathbf{Q}}_d(\theta)}^{-1} \mathbf{C}_{\bar{\mathbf{Q}}_i(\theta)} \end{bmatrix} \bar{\mathbf{Q}}_i(\theta) = \bar{\mathbf{B}} \bar{\mathbf{Q}}_i(\theta). \tag{10}$$

By projecting the first set of equations given in Eq. (9) into the subspace spanned by $\bar{\mathbf{B}}$, one achieves:

$$\mathbf{S}(\theta)\mathbf{Q}(\theta) = \mathbf{F}, \qquad \text{with} \qquad \mathbf{S}(\theta) = \bar{\mathbf{B}}^{\mathrm{T}} \bar{\mathbf{S}}(\theta) \bar{\mathbf{B}} \qquad \text{and} \qquad \mathbf{F} = \bar{\mathbf{B}}^{\mathrm{T}} \bar{\mathbf{F}}, \tag{11}$$

since $\bar{\mathbf{B}}^{\mathrm{T}} \mathbf{C}_{\bar{\mathbf{Q}}(\theta)}^{\mathrm{T}} \boldsymbol{\lambda}(\theta) = \mathbf{0}$. One notes that $\bar{\mathbf{S}}(\theta)$ being symmetric implies the symmetry of $\mathbf{S}(\theta)$. Also, for the unit cell shown in Fig. 1a, the size of $\mathbf{S}(\theta)$ equals 20×20.

2.3 Dynamic behavior of infinite and finite multilayer periodic beams

Free wave propagation in infinite media is commonly described using dispersion diagrams. In the case of periodic structures, such diagrams can be obtained by modeling a single unit cell with the SEM and applying the Bloch–Floquet

theorem, which yields the standard eigenproblem (Mencik, 2010): $\left(\mathbf{S} - \mu_j \mathbf{I}\right) \boldsymbol{\phi}_j = \mathbf{0}$, where μ_j and $\boldsymbol{\phi}_j$, $j = 1, 2, ...$ denote the Bloch eigen-solutions, i.e., the propagation constant and the wave vector, respectively. The corresponding Bloch wave-numbers are obtained by $k_j = (\ln \mu_j)/(-\mathrm{i}\Delta)$, with Δ being the length of the unit cell along the direction of wave propagation, and $\mathrm{i} = \sqrt{-1}$ denotes the imaginary unit. In this context, it should be noted that the deterministic version of the unit cell transfer matrix $\mathbf{S}$ is adopted, since the Bloch–Floquet theorem is strictly applicable only to periodic structures. Accordingly, $\mathbf{S}$ is obtained using the mean values of the stochastic parameters. This choice enables the extraction of relevant insights related to uncertainty quantification, as discussed in more detail in Section 3.1.

On the other hand, the steady state dynamic behavior of stochastic finite periodic structures can be characterized by means of frequency response functions. In particular, transmissibilities ($\mathrm{T}_{ij}(\theta)$) are often used to quantify how vibrations are transmitted through a system, measuring the attenuation characteristics between DoFs i and j. Accordingly, they might be obtained as (Santos *et al.*, 2025):

$$\mathrm{T}_{ij}(\theta) = \frac{H_{ij}(\theta)}{H_{jj}(\theta)}, \tag{12}$$

where H_{ij} and H_{jj} are transfer and driving harmonic forced responses (receptances, mobilities, accelerances), respectively, obtained by the SEM.

3. RESULTS AND DISCUSSIONS

The next subsections describe the investigation of the dynamic behavior of a beam-like PC with attached composite patches. First, deterministic analyses are conducted in Section 3.1. To enable a more comprehensive characterization of the influences exerted by the sources of uncertainty, the stochastic analyses are divided into four subsections. Section 3.2.1 considers randomness in the stacking angle, keeping the remaining variables deterministic. Section 3.2.2 takes into account the random effects only from the gluing position of the composite patch. Section 3.2.3 analyzes the effects of uncertainties regarding the glue material properties, solely. Finally, Section 3.2.4 combines all random sources considered in this work.

3.1 Deterministic analyses

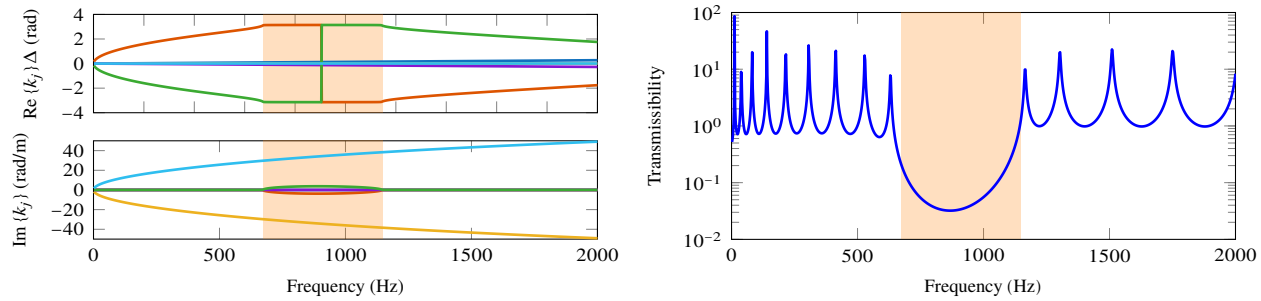
The numerical simulations that follow consider an aluminum host beam periodically covered with composite patches made of epoxy resin and carbon fibers. The aluminum host beam has a rectangular cross-section with dimensions 31.5 mm× 3 mm. Each laminate patch, which covers the full width of the beam, comprises eight layers ($N_\mathrm{p} = 8$), each of them having a thickness of 0.325 mm. For the host beam, the adopted values for the mechanical properties are: Young's modulus $E = 69\,\mathrm{GPa}$, mass density $\rho = 2750\,\mathrm{kg\,m^{-3}}$ and Poisson's ratio $\nu = 0.3$. In addition, the Timoshenko shear correction factor was set to $\kappa = 5/6$. For the composite patches, the following values were adopted: $E_1 = 86.6\,\mathrm{GPa}$, $E_2 = 4.9\,\mathrm{GPa}$, $G_{12} = G_{23} = G_{31} = 1.89\,\mathrm{GPa}$, $\rho = 1560\,\mathrm{kg\,m^{-3}}$ $\nu_{12} = 0.3$, $\nu_{21} = 0.017$ and $\kappa = 5/6$. The parameters l_c and l_p are kept, respectively, as 100 mm and 60 mm ($l_p/l_c = 60\%$, cf. Fig. 1a), and the layers are stacked in a symmetric 0° configuration, which means that in all layers, the fibers are oriented in the longitudinal direction of the unit cell. Accordingly, thin layers of structural adhesive were considered above and below the host beam, with $h_{SA} = 0.35\,\mathrm{mm}$, and material properties set to $E_{SA} = 1.25\,\mathrm{GPa}$, $\rho_{SA} = 1300\,\mathrm{kg\,m^{-3}}$ and $\nu_{SA} = 0.3$.

By employing the theory reviewed in Section 2.3 and adopting the mean values for all random variables considered in this work, wavenumbers were then computed for the deterministic infinite periodic multilayer beam from Fig. 1a. The obtained dispersion relation illustrated in Fig. 5a demonstrates that the infinite periodic beam possesses a bending-related bandgap within the frequency range of interest, i.e., 672–1146 Hz, indicated by the shaded region.

For the finite structure, which comprises ten unit cells, one assumes an harmonic excitation at the rightmost free node, in the transverse direction, and frequency response functions are obtained considering transverse displacement responses at the excitation point (H_{jj}) and at the leftmost free node (H_{ij}), so that Eq. (12) can be applied to obtain the transmissibility curve from Fig. 5b. As one notes, the bandgap predicted in the dispersion diagram matches the very-low amplitude seen in the transmissibility curve. Accordingly, the stochastic analyses that follow are devoted to this attenuation band, which has the limiting frequencies denoted by $f_\mathrm{L} = 672\,\mathrm{Hz}$ and $f_\mathrm{R} = 1146\,\mathrm{Hz}$. With the aim to assess the influence of random variables in the width and central frequency associated with the identified attenuation band, from the transmissibility curve in Fig. 5b, one obtains the amplitudes corresponding to f_L and f_R, which are $\mathrm{T}_\mathrm{L} = 0.219233$ and $\mathrm{T}_\mathrm{R} = 1.10792$, used to identify the attenuation bands in the stochastic samples. In addition, one computes the central frequency of the attenuation zone $f_\mathrm{central} = 909\,\mathrm{Hz}$ and its bandwidth $f_\mathrm{width} = 474\,\mathrm{Hz}$.

3.2 Stochastic analyses

Having established the relevant metrics from the deterministic analyses, the stochastic analysis can now be undertaken in the next subsections.



(a) (b)

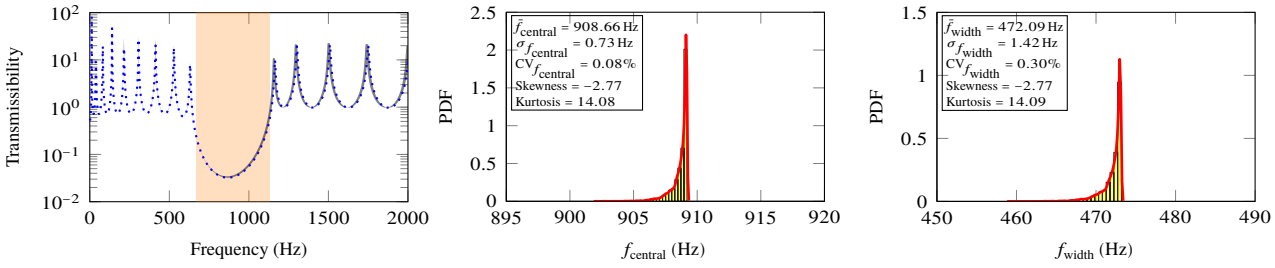
Figure 5: (a) Real and imaginary parts of the dispersion relation for the deterministic multilayer periodic beam, with bandgap highlighted by shaded area. Longitudinal mode (——), bending mode (——), evanescent bending mode (——); (b) amplitudes of the transmissibility function, with the associated attenuation band highlighted.

3.2.1 Randomness in the stacking angles

Stochastic simulations were first performed to assess the effect of the uncertainties in the stacking angle on the attenuation zone of interest (cf. Fig. 1b). As reviewed in Section 2.1, the randomness in SA causes several properties associated with the composite patches to be stochastic, as demonstrated in Eq. (5). For this particular case, the mean value of the Gaussian random variable was set to $\overline{\mathrm{SA}} = [\ 0^\circ\ ]_\mathrm{S}$, with a standard deviation of $\sigma_{\mathrm{SA}} = 1^\circ$. In the Monte Carlo (MC) simulations, 10000 samples were used, which was checked to be enough to guarantee convergence of the outputs.

Accordingly, Fig. 6a shows the mean transmissibility curve obtained from MC simulations along with the corresponding envelope capturing the response variability. The shaded region denotes the frequency interval in which attenuation bands intersect for all samples, defining a common stopband that is robust to parameter uncertainties. On the left of this interval, the response exhibits negligible dispersion, indicating an effectively deterministic behavior. On the right of the attenuation band, the widening envelope reveals increased variability of the dynamic response due to uncertainties in the SA at higher frequencies.

Furthermore, Figs. 6b and 6c demonstrate the probability density functions (PDFs), in solid red lines, estimated using the Kernel's density estimator, superimposed on histograms, as well as some relevant statistics associated with the attenuation zone central frequency and bandwidth, respectively. Although the uncertain inputs were modeled as Gaussian random variables, the resulting output distributions are clearly non-Gaussian, as evidenced by skewness and Kurtosis metrics far from 0 and 3, respectively. Since Gaussianity is preserved under linear transformations, this observation indicates that both f_{central} and f_{width} depend nonlinearly on the underlying random parameter, resulting in a negatively skewed distribution with a long left tail and a sharp data concentration near the upper bound.



(a) (b) (c)

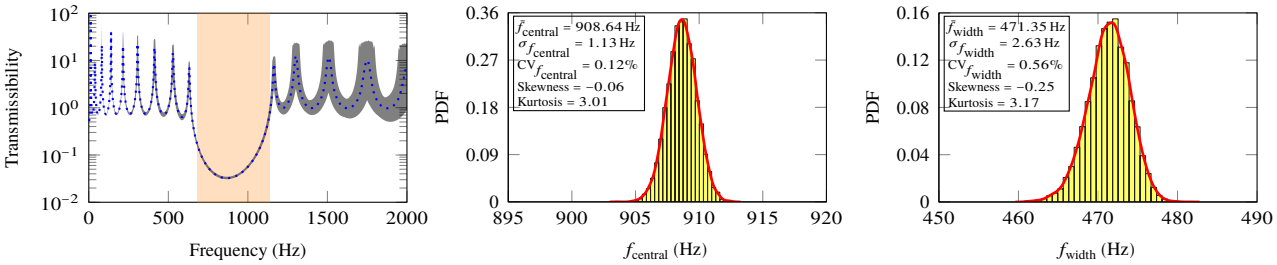
Figure 6: (a) Amplitude of the mean transmissibility function considering 10000 samples, with envelopes of all samples shaded in gray, solely accounting for randomness in the stacking angle; b) histogram, PDF, and statistics of central frequency distribution; c) histogram, PDF, and statistics of bandwidth distribution.

3.2.2 Randomness in the gluing position of the composite patches

In the sequence, stochastic simulations were performed considering randomness only in the gluing position of the composite patch, as demonstrated in Fig. 1c. As this uncertainty is associated with manufacturing imperfections, one random variable was assumed for each unit cell. In this way, the center position of the patch in each unit cell is a random quantity, which can break the periodicity of the whole system and affect wave propagation phenomena. In this case, the mean value of the Gaussian random variable was set to $\overline{\delta}_x = 0$, with a standard deviation of $\sigma_{\delta_x} = 1\,\mathrm{mm}$. Once again,

10000 samples were employed in MC simulations.

Figure 7a illustrates the mean transmissibility curve obtained from the MC simulations, as well as the envelope of all samples. Compared to Fig. 6a, this case demonstrates a higher degree of variability at lower frequencies, on the left of the attenuation band. On the right of this same zone, dispersion is more pronounced than in the previous case, indicating a strong influence of the gluing position on the system's dynamics at higher frequencies. Moreover, Figs. 7b and 7c depict the corresponding PDFs associated with f_{central} and f_{width}, superposed with histograms and some relevant metrics. Unlike the previous case, these distributions resemble Gaussian ones, as evidenced by skewness and Kurtosis near 0 and 3, respectively. Regarding their mean values, both are close to what was observed in the previous case.



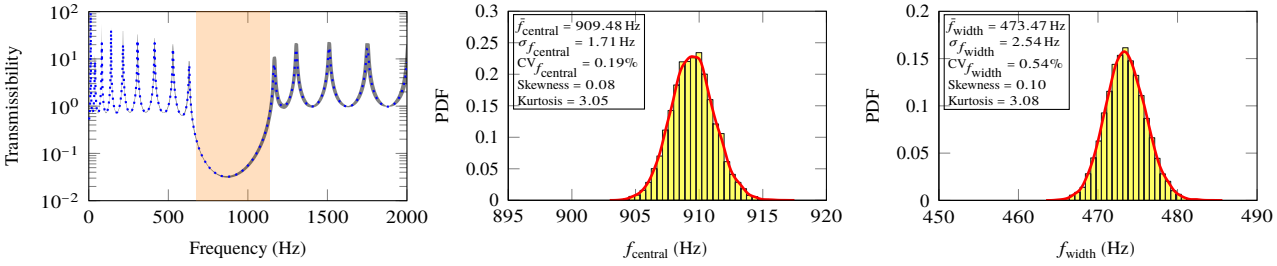
(a) (b) (c)

Figure 7: (a) Amplitude of the mean transmissibility function considering 10000 samples, with envelopes of all samples shaded in gray, solely accounting for randomness in the gluing position; b) histogram, PDF, and statistics of central frequency distribution; c) histogram, PDF, and statistics of bandwidth distributions.

3.2.3 Randomness in the glue material properties

In this case, only uncertainties in the adhesive material properties were considered (cf. Fig. 1d). The thickness h_{SA} was modeled independently for the upper and lower layers of each of the ten unit cells, resulting in twenty random variables. Additionally, three random variables were assigned to E_{SA}, ρ_{SA}, and ν_{SA}, assumed invariant across layers and cells. These variables were sampled 10000 times to evaluate their combined effect on the position and width of the attenuation band. Their mean values, standard deviations and coefficient of variation (CV) were set to: $\overline{h}_{SA} = 0.35\,\text{mm}$, $\sigma_{h_{SA}} = \text{CV}_{h_{SA}}\overline{h}_{SA}$, with $\text{CV}_{h_{SA}} = 20\%$; $\overline{E}_{SA} = 1.25\,\text{GPa}$, $\sigma_{E_{SA}} = \text{CV}_{E_{SA}}\overline{E}_{SA}$, with $\text{CV}_{E_{SA}} = 2\%$; $\overline{\rho}_{SA} = 1300\,\text{kg m}^{-3}$, $\sigma_{\rho_{SA}} = \text{CV}_{\rho_{SA}}\overline{\rho}_{SA}$, with $\text{CV}_{\rho_{SA}} = 1\%$; and $\overline{\nu}_{SA} = 0.3$, $\sigma_{\nu_{SA}} = \text{CV}_{\nu_{SA}}\overline{\nu}_{SA}$, with $\text{CV}_{\nu_{SA}} = 2\%$.

From Fig. 8a, one observes a slightly higher data dispersion on the left and right of the attenuation band compared to the first case (uncertainty in the SA). However, when comparing to the effect of uncertainty in the gluing position, one observes that the impact of the glue material properties are less pronounced. As for the PDFs, Figs. 8b and 8c show they also resemble Gaussian ones, as observed for the randomness in the gluing position case, with a similar dispersion compared to data shown in Figs. 7b and 7c.



(a) (b) (c)

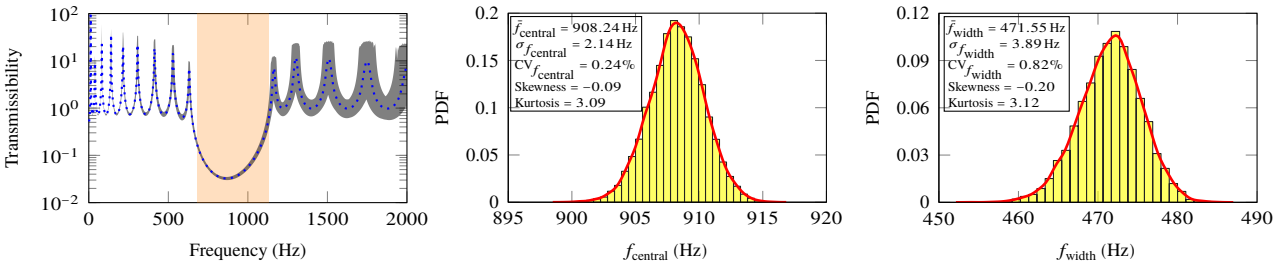
Figure 8: (a) Amplitude of the mean transmissibility function considering 10000 samples, with envelopes of all samples shaded in gray, solely accounting for randomness in the glue material properties; b) histogram, PDF, and statistics of central frequency distribution; c) histogram, PDF, and statistics of bandwidth distributions.

3.2.4 Combined randomness (stacking angle, gluing position of the composite patch, and glue material properties)

Finally, the combined randomness of all stochastic variables are considered in this section in order to assess their joined effects on the central frequency and bandwidth of the attenuation zone. MC simulations were performed with 10000 samples considering the mean values and standard deviations aforementioned for the individual cases. As a result,

comparing Fig. 9a and Fig. 7a, one notes that the effect of the gluing position dominates the dispersion in the transmissibility curve, since a similar behavior can be observed for the combined case. Moreover, the higher-frequency dispersion suggests a stronger influence of variabilities on the second attenuation zone, which is beyond the scope of this study.

From Figs. 9b and 9c, one notes that both distributions exhibit Gaussian patterns, with the highest dispersion in terms of the statistics associated with the outputs among all cases. Thereby, one concludes that manufacturing imperfections and material quality affect the vibration attenuation performance of PC designed with attached composite patches.



(a) (b) (c)

Figure 9: (a) Amplitude of the mean transmissibility function considering 10000 samples, with envelopes of all samples shaded in gray, accounting for all combined randomness; b) histogram, PDF, and statistics of central frequency distribution; c) histogram, PDF, and statistics of bandwidth distributions.

4. SUMMARY AND CONCLUDING REMARKS

In this article, a spectral-based model was proposed for the analysis of beam-like PCs featuring periodically distributed composite laminate patches, to explore composite materials with uncertainty quantification in PC design. Three stochastic sources were investigated: randomness in patch gluing position, stacking angle, and structural adhesive properties. The unit cell model features three spectral elements, in which the carbon fiber patches in the second unit-cell spectral element were initially modeled using ESL to derive their equivalent properties. They were then coupled to the host beam using a multi-layer beam model that accounts for Zig-Zag kinematics, which also considered two additional thin layers to model the structural adhesive. Accordingly, Lagrange multipliers were used to couple the three spectral elements in the unit cell model to obtain final equations of motion, which are subsequently invoked by the SEM. At first, a deterministic case was considered, employing the mean values for all random quantities, to obtain relevant parameters, including the frequency and amplitude associated with the bending-related bandgap and the corresponding attenuation band, respectively. Afterward, stochastic analyses were performed, in a first approach, considering the influence of each random variable separately. In these cases, one perceived a strong asymmetry regarding the distributions of f_{central} and f_{width} when SA was considered stochastic, evidenced by negative skewness and high Kurtosis, which indicates nonlinear relationship between the SA and the outputs. In the remaining individual cases, the distributions resemble Gaussian ones, but with greater dispersion, as demonstrated by the distributions showing randomness only in the gluing position. In the combined case, one observes that the influence of the gluing position dominates data dispersion, with the highest dispersion in terms of the statistics associated with the outputs among all cases. Overall, the study demonstrates that manufacturing-related uncertainties affect the attenuation band characteristics and should be carefully controlled in PC design with composite materials.

5. ACKNOWLEDGMENTS

The authors are grateful to the Brazilian Coordination for the Improvement of Higher Education Personnel (CAPES), the Brazilian National Council for Scientific and Technological Development (CNPq), and the São Paulo Research Foundation (FAPESP) for their continued support to the authors' works. In particular, the authors acknowledge FAPESP for the thematic grant #2018/15894-0, related to the "Periodic structure design and optimization for enhanced vibroacoustic performance: ENVIBRO" research project. V. M. S. Santos acknowledges FAPESP for the grants #2023/11207-7 and #2024/07549-2. D. A. Rade acknowledges CNPq (grant #312068/2020-4) and FAPESP (grant #2021/11258-5, project FLYMOV) for the financial support to his research work.

6. REFERENCES

Abrate, S. and Di Sciuva, M., 2017. "Equivalent single layer theories for composite and sandwich structures: A review". *Compos. Struct.*, Vol. 179, pp. 482–494. doi:10.1016/j.compstruct.2017.07.090.

Agrawal, G., Gupta, A., Chowdhury, R. and Chakrabarti, A., 2022. "Robust topology optimization of negative poisson's ratio metamaterials under material uncertainty". *Finite Elem. Anal. Des.*, Vol. 198, p. 103649. doi:https://doi.org/10.1016/j.finel.2021.103649.

Banerjee, J., Cheung, C., Morishima, R., Perera, M. and Njuguna, J., 2007. "Free vibration of a three-layered sandwich beam using the dynamic stiffness method and experiment". *Int. J. Solids Struct.*, Vol. 44, No. 22–23, pp. 7543–7563. doi:10.1016/j.ijsolstr.2007.04.024.

Billon, K., Zampetakis, I., Scarpa, F., Ouisse, M., Sadoulet-Reboul, E., Collet, M., Perriman, A. and Hetherington, A., 2017. "Mechanics and band gaps in hierarchical auxetic rectangular perforated composite metamaterials". *Compos. Struct.*, Vol. 160, pp. 1042–1050. doi:10.1016/j.compstruct.2016.10.121.

Birman, V. and Kardomateas, G.A., 2018. "Review of current trends in research and applications of sandwich structures". *Composites Part B: Engineering*, Vol. 142, pp. 221–240. doi:10.1016/j.compositesb.2018.01.027.

Bishay, P.L. and Amirbekyan, A.J., 2021. "Design of periodic laminated composite beams in free vibration". *Structures*, Vol. 34, pp. 2030–2040. doi:10.1016/j.istruc.2021.08.071.

Bishay, P.L. and Rodriguez, J., 2021. "Analysis of periodic laminated fiber-reinforced composite beams in free vibration". *J. Vib. Control*, Vol. 28, No. 21–22, pp. 3245–3256. doi:10.1177/10775463211028683.

Carrera, E., 2003. "Historical review of Zig-Zag theories for multilayered plates and shells". *Appl. Mech. Rev.*, Vol. 56, No. 3, pp. 287–308. doi:10.1115/1.1557614.

Fabro, A.T., Meng, H. and Chronopoulos, D., 2020. "Uncertainties in the attenuation performance of a multi-frequency metastructure from additive manufacturing". *Mech. Syst. Signal Pr.*, Vol. 138, p. 106557. doi:https://doi.org/10.1016/j.ymssp.2019.106557.

Huang, B., Li, Q., Shi, W. and Wu, Z., 2007. "Eigenvalues of structures with uncertain elastic boundary restraints". *Appl. Acoust.*, Vol. 68, No. 3, pp. 350–363. doi:https://doi.org/10.1016/j.apacoust.2006.01.012.

Jin, Y., Jia, X.Y., Wu, Q.Q., He, X., Yu, G.C., Wu, L.Z. and Luo, B., 2022. "Design of vibration isolators by using the Bragg scattering and local resonance band gaps in a layered honeycomb meta-structure". *J. Sound Vib.*, Vol. 521, p. 116721. doi:10.1016/j.jsv.2021.116721.

Korshunova, N., Papaioannou, I., Kollmannsberger, S., Straub, D. and Rank, E., 2021. "Uncertainty quantification of microstructure variability and mechanical behavior of additively manufactured lattice structures". *Comput. Method. Appl. M.*, Vol. 385, p. 114049. doi:https://doi.org/10.1016/j.cma.2021.114049.

Lee, U., 2009. *Spectral Element Method in Structural Dynamics*. Wiley. doi:10.1002/9780470823767.

Lee, U. and Kim, J., 2000. "Determination of nonideal beam boundary conditions: a spectral element approach". *AIAA journal*, Vol. 38, No. 2, pp. 309–316.

Mencik, J.M., 2010. "On the low- and mid-frequency forced response of elastic structures using wave finite elements with one-dimensional propagation". *Comput. Struct.*, Vol. 88, No. 11–12, pp. 674–689. doi:10.1016/j.compstruc.2010.02.006.

Reddy, J.N., 2003. *Mechanics of Laminated Composite Plates and Shells*. CRC Press. doi:10.1201/b12409.

Ribeiro, L.H.M., Claeys, C., Fabro, A.T., Chronopoulos, D. and Arruda, J.R.F., 2024. "Robust optimization of a 3d printed periodic frame structure using the inferred characterization of the additive manufacturing system". *Mech. Syst. Signal Pr.*, Vol. 217, p. 111515. doi:10.1016/j.ymssp.2024.111515.

Salatovic, S., Krumscheid, S., Wittemann, F. and Kärger, L., 2025. "Reliable uncertainty quantification for fiber orientation in composite molding processes using multilevel polynomial surrogates". *Probabilist. Eng. Mech.*, Vol. 81, p. 103806. doi:https://doi.org/10.1016/j.probengmech.2025.103806.

Santos, V.M.S., A. D. Martins, Y., E. A. A. Santos, H., de P. Sales, T. and A. Rade, D., 2025. "Stochastic modeling of periodic beams under uncertain boundary conditions and environmental fluctuations". *Int. J. Mech. Sci.*, Vol. 285, p. 109779. doi:10.1016/j.ijmecsci.2024.109779.

Sharma, G.S., Faverjon, B., Dureisseix, D., Skvortsov, A., MacGillivray, I., Audoly, C. and Kessissoglou, N., 2020. "Acoustic performance of a periodically voided viscoelastic medium with uncertainty in design parameters". *J. Vib. Acoust.*, Vol. 142, No. 6, p. 061002. doi:10.1115/1.4046859.

Souza, M.R., Beli, D., Ferguson, N.S., de F. Arruda, J.R. and Fabro, A.T., 2020. "A bayesian approach for wavenumber identification of metamaterial beams possessing variability". *Mech. Syst. Signal Pr.*, Vol. 135, p. 106437. doi:https://doi.org/10.1016/j.ymssp.2019.106437.

Unal, A., Wang, G. and Zuo, Q.H., 2016. "Modeling and analysis of multilayered elastic beam using spectral finite element method". *J. Vib. Acoust.*, Vol. 138, No. 4. doi:10.1115/1.4033355.

Zhang, G.Y., Gao, X.L., Bishop, J.E. and Fang, H.E., 2018. "Band gaps for elastic wave propagation in a periodic composite beam structure incorporating microstructure and surface energy effects". *Compos. Struct.*, Vol. 189, pp. 263–272. doi:10.1016/j.compstruct.2017.11.040.

Zhang, Y., Xu, C., Liu, P., Xie, J., Han, Y., Liu, R. and Chen, L., 2024. "One-dimensional deep convolutional autoencoder active infrared thermography: Enhanced visualization of internal defects in frp composites". *Composites Part B: Engineering*, Vol. 272, p. 111216. doi:10.1016/j.compositesb.2024.111216.

7. RESPONSIBILITY NOTICE

The authors are solely responsible for the printed material included in this paper.